

# Quantitative Emission Spectroscopy for Superorbital Re-entry in the Expansion Tube X2

Tobias Hermann<sup>a</sup>, Stefan Löhle<sup>b</sup>, Uwe Bauder<sup>c</sup>, and Stefanos Fasoulas<sup>d</sup>  
*Universität Stuttgart, Institut für Raumfahrtssysteme,  
Pfaffenwaldring 29, Stuttgart, Germany, D-70569*

Han Wei<sup>e</sup> and Richard Morgan<sup>f</sup>  
*The University of Queensland, Brisbane,  
Centre for Hypersonics, Cooper Rd, St Lucia, 4072, Australia*

A superorbital re-entry flow was realized in the X2 expansion tunnel of the Centre for Hypersonics of the University of Queensland resulting in measurements of electronic excitation temperature, electron density, and particle densities of neutral and ionized atomic nitrogen and oxygen. A rectangular cold wall model is exposed to a flow corresponding to a 12.2 km/s flight equivalent velocity. Vacuum ultraviolet optical emission spectroscopy in the wavelength range between 116 and 185 nm is conducted through a window at the stagnation point. Spatially resolved optical emission spectroscopy of the stagnation streamline in the near infrared wavelength range from 695 to 880 nm is conducted analyzing the flow from the side. Population densities of excited atomic states, electronic excitation temperatures, and electron and ion densities are determined by analyzing the radiative transport in the flowfield. Additionally, the flowfield is numerically simulated using the code URANUS. Agreement in electron density ( $\pm 6\%$ ) and electron temperature ( $\pm 8\%$ ) in the equilibrium region is observed between the numerical simulations and the measurement. Significant differences between measurement and simulation in the distribution of the electron temperature at

<sup>a</sup> PhD student, High Enthalpy Flow Diagnostic Group, IRS, Member AIAA

<sup>b</sup> Research Scientist, High Enthalpy Flow Diagnostic Group, IRS, Member AIAA

<sup>c</sup> Research Scientist, Numerical Modeling and Simulation, IRS, Member AIAA

<sup>d</sup> Professor, Director, IRS, Senior Member AIAA

<sup>e</sup> PhD student, Centre for Hypersonics, University of Queensland

<sup>f</sup> Professor, Director, Centre for Hypersonics, University of Queensland

the shock are attributed to the modeling of the URANUS electron temperature.

### Nomenclature

$A_{ul}$	= Einstein coefficient, $s^{-1}$
$c$	= speed of light in vacuum, m/s
$d$	= diameter, mm
$E$	= state energy, $cm^{-1}$
$f$	= focal length, mm
$g$	= state degeneracy
$h$	= Planck constant, Js
$k$	= Boltzmann constant, J/K
$L_{\lambda}$	= spectral radiance, $W/(m^2 \text{ nm sr})$
$L_{\lambda, \text{Limit}}$	= black body limit spectral radiance, $W/(m^2 \text{ nm sr})$
$m_e$	= electron mass, kg
$n$	= number density, $m^{-3}$
$n_i$	= excited state population density, $m^{-3}$
$P$	= spectral lineshape, $nm^{-1}$
$Q$	= partition function
$T$	= temperature, K
$x$	= distance from the model surface, mm
$\alpha_{\lambda}$	= spectral absorption coefficient, $m^{-1}$
$\varepsilon_{\lambda}$	= spectral emission coefficient, $W/(m^3 \text{ nm sr})$
$\eta$	= virtual population density, $m^{-3}$
$\Lambda$	= thermal electron wavelength, m
$\lambda$	= wavelength, nm
$\tau$	= ionization relaxation time, s

### *Subscripts*

BBL	= black body limit
EQ	= equilibrium
e	= electronic
exc	= electronic excitation
ion	= ionic
l	= lower state
rot	= rotational
tot	= total
trans	= translational
u	= upper state
vib	= vibrational
$\infty$	= at ionization energy

### *Superscripts*

B	= Boltzmann distributed
---	-------------------------

## **I. Introduction**

Space vehicles re-entering the Earth's atmosphere are exposed to extreme heat loads originating from the dissipation of the vehicle's kinetic energy into inner energy of the surrounding air due to the strong bow shock. Across this shock front, close to the vehicle's surface, the air is dissociated and partly ionized. This high temperature, chemically reacting plasma impinges on the vehicle's surface [1]. Spacecraft exposed to this heat flux have to be protected by an appropriate heat shield. The design margins of these protective layers are very high, due mainly to uncertainties associated with the correct prediction of the heat flux [2]. The heat load is composed of a convective and a radiative component, both of which are highly dependent on the thermophysical state of the plasma [3–7]. In order to mitigate the uncertainties of these heat fluxes, the aforementioned extreme environments are investigated in ground based experimental facilities, such as plasma wind tunnels

and impulse facilities. Plasma wind tunnels provide the possibility to conduct long duration tests where the thermochemical state of the boundary layer of the re-entry flight is reproduced [8–13]. This enables the testing of heat shield materials in the environment encountered in flight. However, only the stagnation streamline is considered in the similarity to the re-entry flight [14–16]. Impulse facilities are capable of producing high speed flows for very short times which can be used to conduct aerodynamic testing. Such a facility is the X2 expansion tube at the Centre for Hypersonics at the University of Queensland (UQ) [17]. Here the aim is to duplicate the physical processes of the real re-entry flight for the duration of several microseconds, providing a possibility to study the phenomena encountered in these kinds of flows. Quantitative measurement techniques are required to assess the properties of the flows in the ground based facilities in order to, not only experimentally understand the flowfield, but also to provide sufficient data to validate numerical models (see for example results in [18]).

In the present study, optical diagnostic methods are applied to a superorbital re-entry flow with an enthalpy of 74.5 MJ/kg impinging on a cold wall flat faced model (25 mm tall, 90 mm wide). This condition corresponds to a 12.2 km/s flight equivalent velocity and a  $1 \times 10^{-3}$  kg/m<sup>3</sup> free stream density and was previously analyzed in depth by Sheikh and thus providing a benchmark case [19]. The condition is among possible re-entry trajectory points for future sample return missions. Computational analysis of heating rates showed that the radiative heat flux is in the order of, or in excess of the convective heat flux [20]. As the uncertainty of the radiative heating is still very large, the analysis of the thermophysical state of the flow provides the opportunity to study the sources and properties of the radiation in the respective shock layer [2].

In this study, physical parameters of the flow are derived from optical emission spectroscopy (OES). The accessibility of a broad spectral range in a single measurement allows a comparably detailed measurement by providing information on many excited states of different species. Furthermore, spatial resolution along one axis is possible which allows the observation of the development of the flow within the shock layer [21]. On the other hand, only excited states of particles can be detected as these are the ones emitting radiation [22]. Therefore, obtaining total particle densities of a species requires the analysis of the population densities of low energy and ground states, which

is conducted by considering the radiative transport in the flowfield. OES in the near infrared is a well established standard at the Centre for Hypersonics [21, 23, 24]. In addition, with the relatively new vacuum ultraviolet (VUV) spectroscopic system, the spectral range required for the analysis of ground state densities becomes accessible [25, 26].

In this study, the VUV stagnation point spectrum (116-185 nm) is measured through the surface of the sample. The NIR spectrum (695-880 nm) is measured along the stagnation streamline viewing the flow from the side. Measurements of electronic excitation temperature and particle densities of atoms, ions, and electrons (N, O, N<sup>+</sup>, O<sup>+</sup>, e<sup>-</sup>) are presented, these are obtained by analyzing the radiative transport of atomic lines [26–30]. Comparisons are presented between (i) measurement results, (ii) a numerical simulation utilizing equilibrium chemistry (PITOT), and (iii) a detailed numerical simulation utilizing nonequilibrium chemistry, multi-temperature models, and loose radiation coupling (URANUS, HERTA, PARADE) [31, 32].

## II. Experimental facility and spectroscopic setup

The facility used in this study is the free-piston compressed-gas-driven expansion tube X2 in the configuration with a single driver tube, a 85 mm diameter acceleration tube and a 208 mm diameter nozzle. The flow parameters used corresponding to a 12.2 km/s flight equivalent velocity are reproduced from the work of Sheikh and are outlined in Table 1 [19]. The values designated with the term 'calculated' are the result of a numerical simulation with the chemical equilibrium code PITOT which utilizes the chemical equilibrium with applications (CEA) lookup tables [31, 33].

A flat faced two-dimensional model of 25 mm height and 90 mm width was used. The model features an optical access through a MgF<sub>2</sub> window embedded flush in the surface at the stagnation point allowing VUV radiation to enter the evacuated optical path. The light is then redirected out of the test section and focused (focusing mirror focal length  $f = 500$  mm, aperture diameter  $d = 30$  mm, magnification 0.85) onto the entrance slit of a McPherson NOVA 225 normal incidence spectrometer with a focal length of 1 m coupled to an Andor iStar generation 2 intensified charge coupled device (ICCD). A slit width of 25  $\mu$ m, a 3001/mm grating set to a center wavelength of 150 nm, an intensifier gain of 4000, and an exposure time of 4  $\mu$ s was used to acquire the VUV spectra. The recording was triggered 60  $\mu$ s after the arrival of the initial shock which is detected

**Table 1 Freestream test conditions calculated using PITOT and available measured values [19].**

Parameter	Calculated	Measured
Primary shock velocity, km/s	5.64	$5.70 \pm 0.15$
Secondary shock velocity, km/s	11.7	$11.50 \pm 0.40$
Static pressure at nozzle entry, Pa	4460	$7000 \pm 1800$
Pitot pressure, kPa	135	$140 \pm 28$
Test gas velocity, km/s	11.8	N/A
Test gas temperature, K	2800	N/A
Test gas Mach number, km/s	11.9	N/A
Test gas density, kg/m <sup>3</sup>	$1.00 \times 10^{-3}$	N/A
Test gas enthalpy, MJ/kg	74.5	N/A
Test gas static pressure, Pa	870	N/A

by a photodiode. The flowfield in front of the model is then considered to be fully established. The measured wavelength range covers 116 to 185 nm with a resolution of 0.06 nm/px. A detailed description of the complete system is available in the work of Sheikh [19].

Additionally, the flow is viewed from the side by a NIR spectroscopic setup. Light emitted in the flow passes through a UV grade fused silica window and is focused (focusing mirror focal length  $f = 500$  mm, aperture diameter  $d = 10$  mm, magnification 0.85) onto the entrance slit of an Acton SpectraPro 2358i spectrometer coupled to a Princeton Instruments PI-MAX ICCD camera. Furthermore, the light beam is rotated by a periscope arrangement in front of the spectrometer entrance slit such that the direction of the slit is aligned horizontally with the stagnation streamline. A slit width of  $50 \mu\text{m}$ , a 150 l/mm grating set to a center wavelength of 800 nm, an intensifier gain of 200, and an exposure time of  $2 \mu\text{s}$  was used to acquire the NIR spectra. The delay of the recording after the arrival of the initial shock is also  $60 \mu\text{s}$  so that VUV and NIR spectra are acquired from the same flow. The measured wavelength range covers 695 to 880 nm with a resolution of 0.55 nm/px. This setup is based on the work of Eichmann [21]. A schematic of both spectroscopic systems is presented in Fig. 1.

In addition to the spectroscopic measurements, the flow is monitored with a Shimadzu Hy-

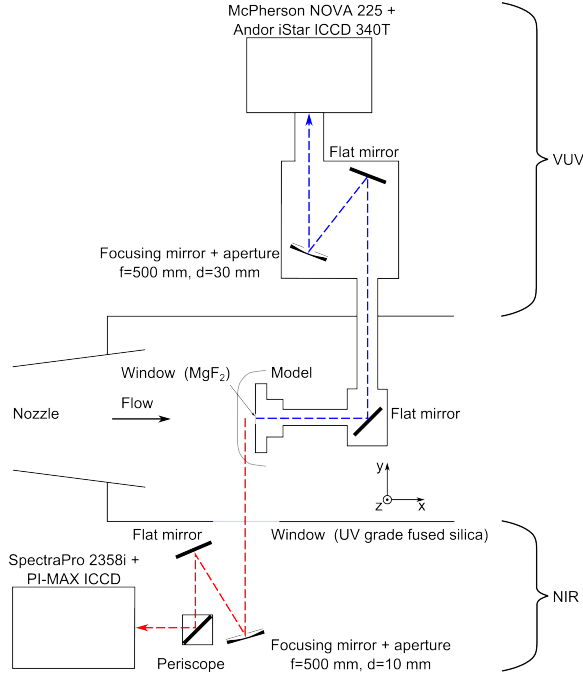


**Fig. 1 Top view of the schematic setup of the spectroscopic systems.**

pervision HPV-1 high speed camera viewing the model from the top, i. e. the  $z$ -axis in Fig. 1. A Thorlabs FBH780-10 bandpass filter is used so that only the atomic oxygen 777.55 nm multiplet is recorded [34].

The VUV spectroscopic system is calibrated using a McPherson model 632 deuterium lamp for absolute spectral radiance by placing it directly in front of the model and thus accounting for all optical components in the light path [19]. The NIR system was also calibrated for absolute spectral radiance using a tungsten calibration lamp, OL 200M. The calibration is conducted following the methodology of McIntyre et al. [24]. The losses of each individual optical component are measured according to the procedure depicted in the work of Jacobs [35]. The determination of the spatial resolution of the NIR measurements is conducted by dividing the known pixel size of the ICCD camera by the system magnification yielding 0.031 mm/px.

Figure 2 shows the calibrated stagnation point spectrum in the VUV region covering the 115 to 185 nm wavelength interval. Following the method of Sheikh the contaminant emission is removed, e. g. aluminium and carbon atomic lines [19]. The spectrum is dominated by atomic lines of nitrogen and oxygen. Figure 3 shows the calibrated spectrum in the NIR region from 695 to 880 nm on the

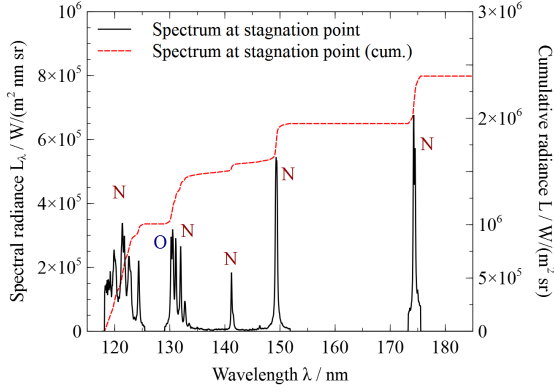


**Fig. 2** Measured stagnation point VUV spectrum (116-185 nm).

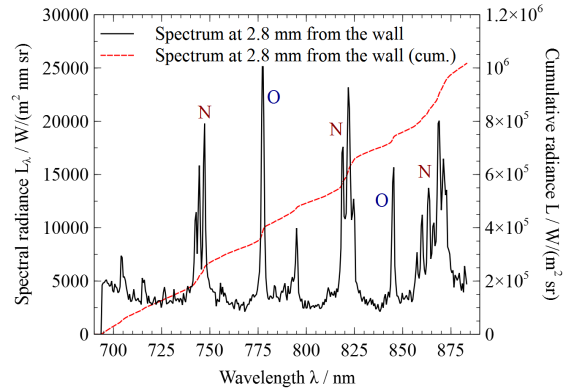


**Fig. 3** Measured NIR spectrum (695-880 nm) at 2.8 mm in front of the model surface.

stagnation streamline at 2.8 mm in front of the model surface. It is evident that this spectral region is also dominated by atomic radiation of nitrogen and oxygen. Furthermore, a continuous background is present in the spectrum which adds a significant portion to the cumulative radiance in this spectral interval. However, it is yet unclear whether this background can be solely attributed to continuum radiation of free-free and bound-free transitions. As recently pointed out by Brandis et al., a blending together of line wings due to the spectrometer instrument function, e. g. the spreading of lines by the intensifier in front of the CCD chip, might also contribute to the elevated background radiation [36]. This deceiving effect is especially prominent at low spectral resolution as is the case in the NIR measurements. Another possible source of the continuous background is Planck radiation stemming from heated particles in the flow, such as soot or diaphragm material. The calibrated measured spectra are further analyzed in the following section.

### III. Analysis methodology

This section presents an overview of the different methods used to derive the thermodynamic properties of the flow through the detailed analysis of the emission features in the two spectral regions measured. The analysis only considers the atomic species of nitrogen and oxygen, their respective ions, and free electrons. Figure 4 depicts the overall analysis procedure.

The overall scheme is iterative as the knowledge of some output parameters is required as an input. Therefore, the whole procedure is conducted iteratively until convergence is obtained. First,

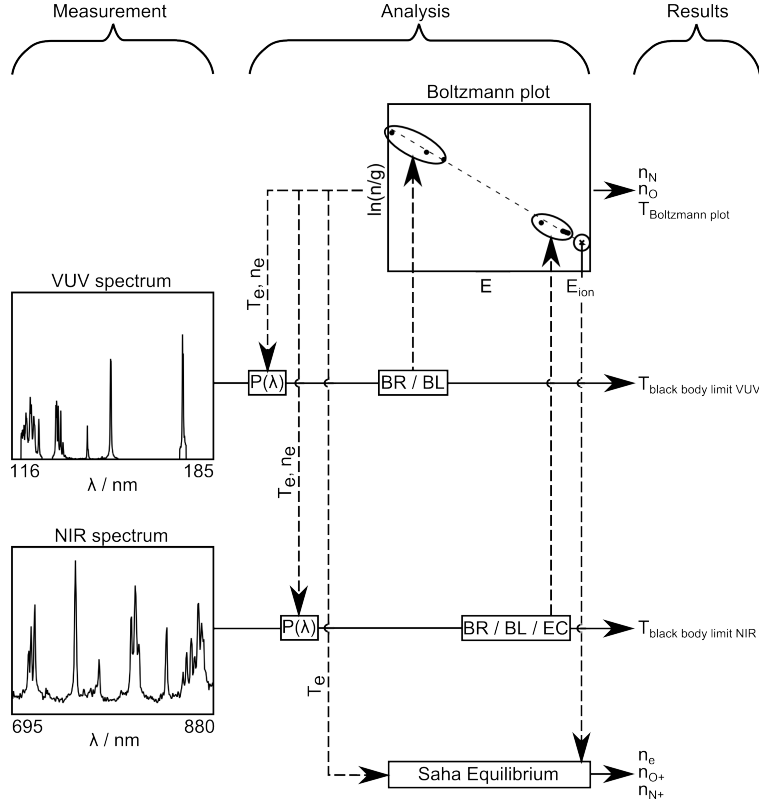


**Fig. 4 Schematic of the analysis procedure. (BR) Branching ratio, (BL) black body limit, (EC) emission coefficient.**

the black body temperature is obtained from the VUV spectrum and an estimated lineshape  $P(\lambda)$  for each spectral line (described in section III B 1) [29, 37]. The analysis of the branching ratio of atomic multiplets in the VUV allows the determination of low energy state population densities (described in section III A 1) [38–40]. Furthermore, the black body limiting curves are used to extrapolate to other low energy states (described in section III A 3) [26]. Boltzmann distributed atoms always have the largest amount of particles in low energy states. Therefore, summing over those states results in a total number density estimate of the respective atom. Electron and ion densities are then determined assuming a Saha equilibrium (described in section III C) [30]. The Boltzmann plot allows to determine the electronic excitation temperature through the slope of the excited state distribution (see Fig. 4 upper plot, described in section III B 2) [27]. The measured electronic excitation temperature and electron density are then used to calculate the lineshape of each line in the NIR [41, 42]. It has been found out that the NIR is also black body limited and is thus strongly

self absorbing. A black body limit temperature is obtained by using the calibrated spectrum and the respective lineshape of each line (described in section III B 1). A self-absorption correction of NIR multiplets is conducted to obtain the upper state population density of the respective lines by applying the methodology of Fletcher (described in section III A 2) [27]. A branching ratio analysis of NIR multiplets is used to determine the lower state population density which, in the case of the NIR spectral region, is still a highly excited state (described in section III A 1). With both high and low energy states available a wide energy interval of the Boltzmann plot is considered. This significantly improves the accuracy of the calculation of electronic excitation temperature, and the electron and ion densities. These values are then used to compute the VUV lineshape and the complete procedure is repeated. In the following, the individual analysis methods are presented in more detail.

#### A. Atomic states population density measurements

Different atomic energy states are measured by analyzing the radiative transport of multiplets in the flowfield. The different methods are presented below.

##### 1. Lower state population density determination by branching ratio analysis

Within a single emission multiplet, the relative intensity between different lines, i. e. the branching ratio, is entirely determined by spectroscopic constants. Deviations from this fixed ratio occur due to self-absorption processes in the plasma. The branching ratio method allows the determination of the lower state of a transition by analyzing the characteristic shape of a self-absorbed multiplet [38–40]. Different absorption strengths of individual lines within the same multiplet cause a different line ratio based on the lower state population density. This method is used for atomic nitrogen and oxygen multiplets in both the VUV and the NIR spectra (see Table 2).

For each multiplet used, the one-dimensional radiative transport in the flowfield is calculated along the line of sight  $s$  of the respective spectroscopic system according to

$$L_{\lambda}(\lambda) = \int_{\text{Shock}}^{\text{Window}} \varepsilon_{\lambda}(\lambda, s) \cdot \exp \left( \int_s^{\text{Window}} \alpha_{\lambda}(\lambda, s) ds \right) ds \quad (1)$$

with the spectral emission coefficient  $\varepsilon_{\lambda}$  and the spectral absorption coefficient  $\alpha_{\lambda}$ . Subsequently,

**Table 2 Atomic multiplets used in this study [43].**

$\lambda_0$ / nm	$A_{ul}$ / s <sup>-1</sup>	$E_l$ / cm <sup>-1</sup>	$E_u$ / cm <sup>-1</sup>	BR <sup>a</sup>	EC <sup>b</sup>	BL <sup>c</sup>
Nitrogen						
120.00	$4.04 \cdot 10^8$	0	83336	×	×	✓
149.33	$3.44 \cdot 10^8$	19228	86193	×	×	✓
124.32	$3.45 \cdot 10^8$	19228	99664	×	×	✓
174.35	$1.25 \cdot 10^8$	28839	86193	✓	×	✓
141.19	$5.39 \cdot 10^7$	28839	99664	×	×	✓
133.59	$3.06 \cdot 10^4$	28839	103693	✓	×	×
132.70	$9.75 \cdot 10^6$	28839	104196	✓	×	✓
131.95	$7.26 \cdot 10^7$	28839	104628	✓	×	✓
131.86	$1.46 \cdot 10^5$	28839	104675	✓	×	✓
131.63	$4.80 \cdot 10^5$	28839	104810	✓	×	✓
131.57	$2.30 \cdot 10^5$	28839	104846	✓	×	✓
131.30	$2.30 \cdot 10^5$	28839	105000	✓	×	×
131.07	$7.73 \cdot 10^7$	28839	105134	✓	×	✓
869.40	$2.53 \cdot 10^7$	83336	94838	✓	✓	×
821.41	$3.08 \cdot 10^7$	83336	95510	✓	✓	×
745.42	$3.71 \cdot 10^7$	83336	96751	✓	✓	×
861.98	$3.16 \cdot 10^7$	86193	97794	×	✓	×
Oxygen						
130.35	$6.12 \cdot 10^8$	78	76795	✓	×	×
777.55	$3.69 \cdot 10^7$	73768	86629	×	✓	×
844.88	$3.22 \cdot 10^7$	76794	88631	×	✓	×

<sup>a</sup> Branching ratio evaluation<sup>b</sup> Self-absorption corrected emission coefficient evaluation<sup>c</sup> Black body limit extrapolation evaluation

the calculated spectrum is convolved with the respective instrument slit function and compared to the measured spectrum. The slit function of the VUV spectroscopic system is obtained from the Lyman- $\alpha$  line in the calibration lamp spectrum. The NIR spectroscopic system slit function is

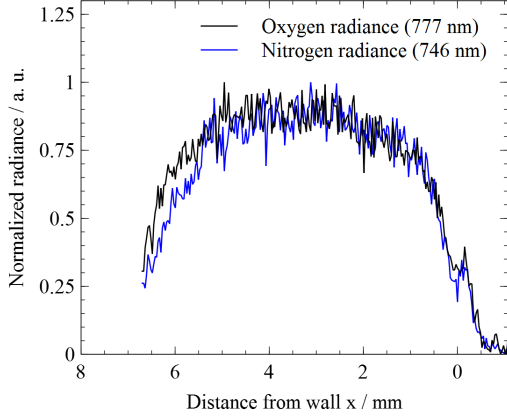


**Fig. 5** Normalized distribution of atomic radiation along the stagnation streamline (NIR spectroscopy measurement).

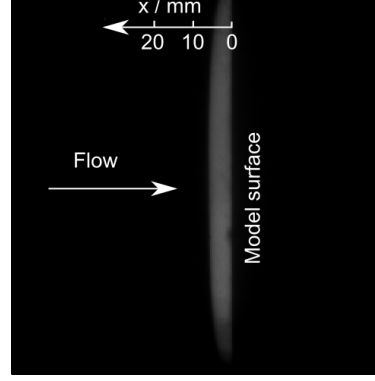


**Fig. 6** High speed camera image with band-pass filter (780 nm (10 nm FWHM)).

obtained from thin lines emitted by the lamps used for laboratory illumination. In the branching ratio analysis, the lower state population density is a variable input parameter which is varied until the best agreement between the calculated and the measured spectra is obtained [26].

The radiative transport calculation requires the distribution of atoms as well as the spectral lineshape along the line of sight (see Eq. (1)). In the case of the NIR spectroscopy, the atomic distribution is assumed to be constant over the width of the flow [24]. In the case of the VUV spectroscopy, the distribution of the measured atomic radiation of NIR multiplets is used (the 777 nm line for oxygen, and the 746 nm line for nitrogen). The resulting normalized distributions are presented in Fig. 5 and a top view of the distribution of the 777 nm line is shown in Fig. 6.

As can be seen in Fig. 5, the first region of the shock layer ( $x > 7.5$  mm) has not been captured in the spectroscopic measurement, but the radiation in this region is very weak (see Fig. 6).

The spectral lineshape is calculated taking into consideration several broadening mechanisms. Van der Waals broadening, accounting for collisions with neutral particles, is calculated based on the empirical correlation from the work of Laux [41], Stark broadening, accounting for collisions with free electrons, is calculated using the correlation given by Johnston et al. [42], and Doppler broadening, accounting for the particle velocity distribution, is calculated by assuming a thermal equilibrium between electronic excitation temperature and translational temperature [41]. The

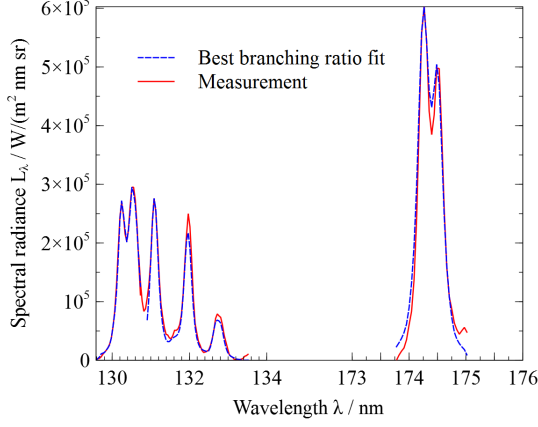


**Fig. 7** Measured and calculated multiplets used for the branching ratio analysis in the VUV.

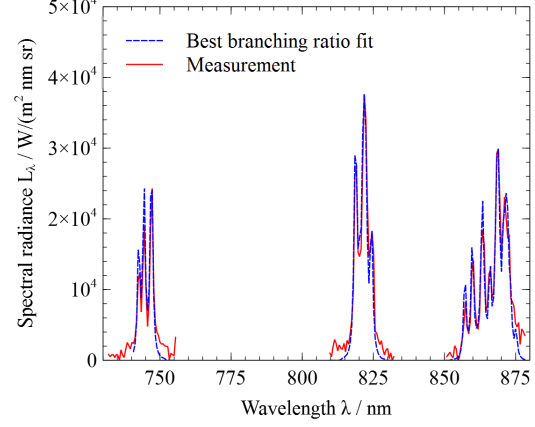


**Fig. 8** Measured and calculated multiplets used for the branching ratio analysis in the NIR.

analysis of the radiative transport of atomic lines in the VUV revealed that the radiation stemming from the nonequilibrium region of the flow has very little significance for the overall measurement signal, since most of it is re-absorbed in the equilibrium region. The biggest part of the measured radiance originates from the equilibrium region and the boundary layer. Therefore, the assumption of an equilibrium between the temperatures of heavy particles and free electrons is made. The measured electron temperature distribution is used for the self-absorption calculation along the line of sight of the VUV system (see Figs. 17 and 18). In the case of the NIR system, the temperature is again assumed to be constant over the width of the flow. Comparing the individual broadening mechanisms, Stark broadening is by far the most dominant contributor.

Figures 7 and 8 show the comparison between the measurement and the best fit of the calculated multiplets with the excited state population densities  $n_N(83336 \text{ cm}^{-1}) = 5.4 \times 10^{19} \text{ m}^{-3}$ ,  $n_N(28839 \text{ cm}^{-1}) = 1.7 \times 10^{22} \text{ m}^{-3}$  and  $n_O(78 \text{ cm}^{-1}) = 8.6 \times 10^{22} \text{ m}^{-3}$ . Background radiation, e. g. free-free or bound-free radiation, of the individual multiplets is excluded from the analysis by removing the baseline of each multiplet, i. e. the minimum value in the respective wavelength region (see Figs. 7 and 8). The agreement between calculation and measurement is excellent in the VUV, while some discrepancies exist in the NIR which can be attributed to the low spectral resolution and the broad instrument function. Another possible source of the discrepancy is nonequilibrium

in the flow.

The branching ratio method works best when a high spectral resolution exists which allows the clear separation of single lines within a multiplet. The more the lines are overlapping, the more influential the instrument slit function becomes which must be accurately known. Furthermore, the number of different multiplets used for the same lower state is important. Due to the different optical depths of individual multiplets, the sensitivity of their respective branching ratios to the lower state number density depends greatly on the thermodynamic regime and the depth of the radiating field. Considering many multiplets of a common lower state increases the overall sensitivity. Due to the complex simulation, error bars are not easily estimated. Laity et al. approximate the uncertainty from branching ratios to be about 50 % [44]. In this work, this percentage is used for all population densities obtained using the branching ratio method.

## 2. Upper state population density by emission coefficient correction for self-absorption

The amount of radiation emitted by a multiplet, i. e. the local emission coefficient, is calculated by

$$\varepsilon = \frac{n_u A_{ul} h c}{4 \pi \lambda_0} \quad (2)$$

and depends only on the energy difference of the transition  $hc/\lambda_0$ , the Einstein coefficient  $A_{ul}$  and the upper state number density  $n_u$  [41]. As the respective spectroscopic constants are known, the local emission coefficient can be used to determine the upper state population density. In environments which are not optically thin, as in the present case, part of the radiation is trapped inside the plasma due to self-absorption processes. Therefore, these absorption processes have to be accounted for when the local emission coefficient is determined, this is done following the methodology of Fletcher [27]. This method is employed on multiplets in the NIR spectral region and results in the population densities of high energy states (see Table 2). As a first step the radiation of the respective multiplets is considered to be optically thin. This allows the calculation of the local emission coefficient by simply dividing the measured spectral radiance by the width of the flow [24]. The local emission coefficient of the respective multiplets is spectrally integrated to determine local

population densities of the respective upper states by using Eq. (2) and the tabulated spectroscopic constants (see Table 2) [41]. The next step is to estimate the lower state population density of each transition from the Boltzmann distribution based on the low energy states obtained by the branching ratio analysis as well as a first guess of the high energy states (refer to Fig. 4). Using this estimate, the amount of radiation trapped by self-absorption in the flowfield is calculated. The upper state population density is then corrected for this trapped amount and the procedure is repeated until convergence is obtained. Possible error sources of this method include uncertainties in the radiative transport calculation, the spectroscopic constants, the calibration lamp data, the magnification and solid angle, the reflectivity of the external optics, and the camera accuracy including thermal and shot noise [45]. The uncertainty analysis of the measured spectral radiance is conducted according to the work of Jacobs [35]. To account for uncertainties in the radiative transport, the calculation is conducted for each multiplet with the maximum and minimum possible line width. The margins of the line width result from the uncertainties in temperature, Stark width and electron density [42]. The overall uncertainty margin is the combination of all discussed influences.

### *3. Lower state population densities by extrapolation using the black body limit*

The self-absorption analysis in the preceding paragraphs revealed that many of the strong VUV multiplets are black body limited, i.e. their peak spectral radiance is limited to a level as defined by a black body radiation according to Planck's law. This has been checked for each multiplet by evaluating the black body limit criterion given by Johnston et al. [46]. In the case of a non-Boltzmann distributed population of the atomic states, each transition is limited by a unique Planck-function applicable only between the respective upper and lower state [47]. These nonequilibrium black body limit curves can be calculated using the work of Johnston et al. [46]. However, the analysis of the energy states measured so far ( $E \geq 28839 \text{ cm}^{-1}$ ) revealed that the population among these is, within the error margins, Boltzmann distributed (see Fig. 11). With this premise for the upper states, the approximation given in Ref. [46] can be re-arranged to calculate the limiting curves in the VUV

using

$$L_{\lambda, \text{Limit}} = \frac{2hc^2}{\lambda^5} \frac{n_l^B}{n_l} \frac{1}{\exp\left(\frac{hc}{\lambda k T_{\text{exc}}}\right) - 1} \quad (3)$$

with the wavelength  $\lambda$ , Planck's constant  $h$ , the speed of light in vacuum  $c$ , Boltzmann's constant  $k$ , the electronic excitation temperature  $T_{\text{exc}}$ , the lower state population density  $n_l$ , and the lower state population density according to a Boltzmann distribution  $n_l^B$ . **The observation that the line maxima follow different Planck limits indicates that the states do not follow the same Boltzmann distribution. As the upper state densities are known, i. e. by the branching ratio method of a different line, or can be related to a nearby known state by a Boltzmann relationship, then the density of the lower state may be determined via the above formula.**

The limiting curve applies to the actual lineshape after the radiative transport, i. e. the lineshape without instrumental broadening. Therefore, the radiative transport for each multiplet is calculated along the line of sight of the VUV spectroscopic system. The resulting lineshape is scaled such that the integral of the calculated multiplet corresponds to the integral of the respective measured multiplet. The result is shown in Fig. 9 [48]. A black body curve is calculated which matches the peaks of the limited lines of the transitions with the  $E=28839 \text{ cm}^{-1}$  lower level. **As the  $E=28839 \text{ cm}^{-1}$  lower level has been shown to be Boltzmann distributed, the resulting limiting curve is a Planck-function without the factor  $n_l^B/n_l$ .** Subsequently, this curve is scaled to best fit the peaks of the transitions with the  $E=19228 \text{ cm}^{-1}$  lower level, and the  $E=0 \text{ cm}^{-1}$  lower level respectively (see Fig. 9). These scaling factors correspond to the deviation from the Boltzmann distribution  $n_l^B/n_l$  in Eq. (3). The population densities of the  $E=19228 \text{ cm}^{-1}$  and  $E=0 \text{ cm}^{-1}$  states are obtained by extrapolating the Boltzmann distribution function (obtained as a best fit for all measured states, compare Fig. 11) and applying the measured deviations from this curve for the two states respectively. The complete procedure is repeated with the deduced lower state number density since the lineshape after the radiative transport is a function of the state densities. This is conducted iteratively until convergence is obtained.

As is evident in Fig 9, the resulting curves are close to each other, i. e. there appears to be no significant deviation from a Boltzmann distribution. One drawback of this method is the

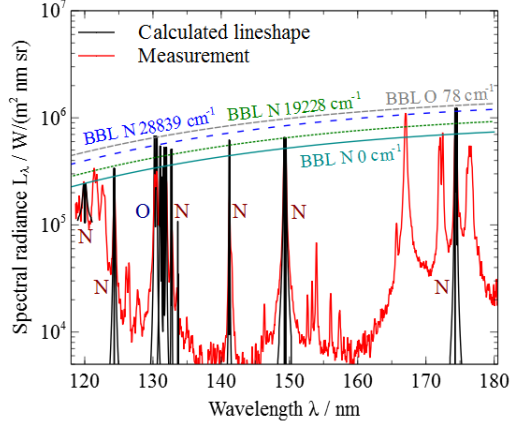


**Fig. 9** Measured VUV spectrum, calculated lineshapes after the radiative transport and black body limiting curves.

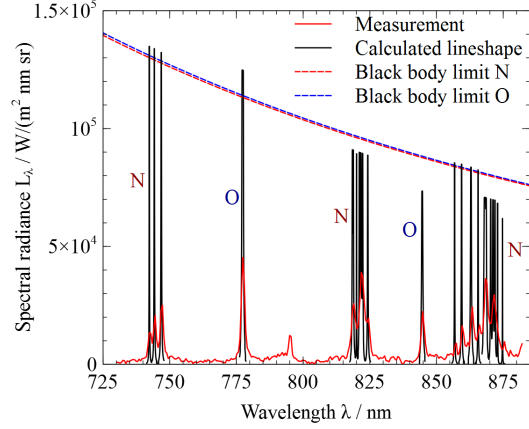


**Fig. 10** Measured NIR spectrum, calculated lineshapes after the radiative transport and black body limiting curves.

uncertainty in the width of the calculated lineshape. As the dominant broadening mechanism is Stark broadening, the significant uncertainty of the literature values (30-100 %) for this mechanism reflects directly on the calculated lineshape [42]. When the line width is broader, the respective peak value is lower as the measured integral is conserved. To quantify the respective uncertainty in population density, the procedure has been applied using the maximum and minimum possible line width for each multiplet, which result from the uncertainties in temperature, Stark width and electron density [42]. The uncertainty of the measured integral of each multiplet is an additional error source. The measurement uncertainty is evaluated accounting for the calibration lamp uncertainty as well as the camera thermal noise and shot noise [45]. Furthermore, the extrapolation to the lower states obeys an exponential relationship and thus introduces an additional source of uncertainty. The uncertainty boundaries of the extrapolation are simply the two bordering lines in the Boltzmann plot that barely lie within the error margins of all measured states that were obtained by the branching ratio and emission coefficient methods (dotted lines in Fig. 11). Thus, the difference between these two bordering lines at the respective energy of the state is applied as the error margin of the extrapolation. The combined uncertainty from all discussed influences is shown in Fig. 11 for the two respective states ( $E=19228 \text{ cm}^{-1}$  and  $E=0 \text{ cm}^{-1}$ ).

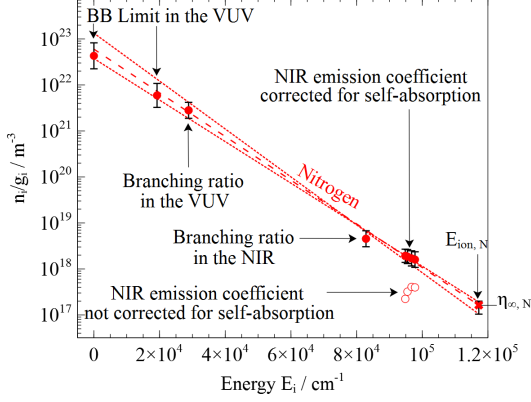


Fig. 11 Atomic nitrogen Boltzmann plot on the stagnation streamline 2.8 mm from the model wall.

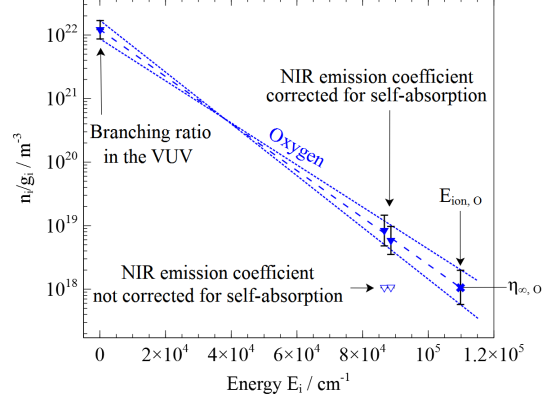


Fig. 12 Atomic oxygen Boltzmann plot on the stagnation streamline 2.8 mm from the model wall.

## B. Temperature measurement

In addition to the measurement of population densities, temperatures are obtained from the analysis of the measured spectra. The two methods applied are described in the following.

### 1. Electronic excitation temperature using the black body limit

The calculated black body limiting curve described in section III A 3 is also used to determine the electronic excitation temperature (see Eq. (3)) [37]. This procedure is applied to both the VUV and the NIR spectra. **In the case of the NIR spectra no extrapolation to lower states is conducted, i. e. Eq. 3 is used without the factor  $n_l^B/n_l$ .** The resulting curves for atomic nitrogen and oxygen are presented in Fig. 9 for the VUV region ( $T_{\text{BBL,VUV,N}} = 12400 \text{ K}$   $T_{\text{BBL,VUV,O}} = 13000 \text{ K}$ ), and in Fig. 10 for the NIR region ( $T_{\text{BBL,NIR,N}} = 11960 \text{ K}$   $T_{\text{BBL,NIR,O}} = 12000 \text{ K}$ ).

For the NIR spectral region, the radiative transport calculation needed to obtain the lineshape is conducted assuming constant properties over the width of the flow. As all nitrogen multiplets considered in the NIR share the same lower level, all of them are used to obtain the best fit of the respective Planck function. Both oxygen multiplets are used for one Planck function fit in order

to mitigate errors introduced through uncertainties in the measurement data. As in the case of the black body limit extrapolation method, uncertainties in Stark broadening are large. However, the temperature determination is less sensitive to these uncertainties. The depicted procedure has again been applied using maximum and minimum line widths in order to quantify the uncertainty stemming from the radiative transport calculation. The uncertainty in absolute radiance of the VUV spectra is calculated considering calibration lamp uncertainty, thermal noise and shot noise of the camera [45]. The NIR absolute radiance uncertainty is calculated accounting for the calibration lamp data, the magnification and solid angle, the reflectivity of the external optics, and the camera accuracy including the thermal and shot noise [35, 45].

## 2. *Electronic excitation temperature using the Boltzmann plot method*

Plotting all the measured population densities in a Boltzmann plot, the electronic excitation temperature is obtained by calculating a best linear fit to all states of the atomic species [27]. The slope of this linear function is directly related to the electronic excitation temperature  $T_{\text{exc}}$  of the respective atom, i. e. this temperature controls the distribution of the different energy states  $i$  of an atom according to

$$\frac{n_i}{g_i} = \frac{n_{\text{tot}}}{Q} \exp\left(-\frac{E_i}{kT_{\text{exc}}}\right) \quad (4)$$

with the population density  $n_i$ , the degeneracy  $g_i$ , the total atom number density  $n_{\text{tot}}$ , the partition function  $Q$ , Boltzmann's constant  $k$  and the state energy  $E_i$  [41]. The Boltzmann plots for atomic nitrogen and oxygen corresponding to the stagnation streamline at 2.8 mm from the model wall are presented in Figs. 11 and 12. The various methods describing how the population densities were obtained are indicated (refer to Fig. 4). Figures 11 and 12 show that both atoms (N and O) are Boltzmann distributed. The large energy range improves the accuracy of the temperature determination by the Boltzmann plot method significantly compared to the standard procedure where only the high energy states are considered. However, uncertainties in the determination of the individual atomic states add uncertainty to the measured slope, i. e. the electronic excitation temperature, of the linear fitted function. The error margins of the temperature determination

correspond to the slopes of the two bordering lines in the Boltzmann plot that barely lie within the error margins of all measured states. Figures 11 and 12 demonstrate the significance of the self-absorption correction for high energy states. The uncorrected values are considerably lower and the distribution is not plausible while the corrected values exhibit a behavior expected from this kind of flowfield [41].

### C. Electron and ion density measurement

This section presents the method used to obtain total number densities of electrons and ions ( $N^+$ ,  $O^+$ ) by assuming a Saha equilibrium between the atoms and their respective ions. Based on the work of van der Sijde et al., the Boltzmann plot is used to extrapolate to a virtual state  $\eta_\infty$  at the ionization energy of the respective atom ( $E_{\text{ion},N} = 117225.7 \text{ cm}^{-1}$ ,  $E_{\text{ion},O} = 109837.02 \text{ cm}^{-1}$ ) [30]. The extrapolated states are depicted in Figs. 11 and 12 and can be applied in the Saha equation using the formulation of van der Sijde et al. [30],

$$\eta_\infty = n_e \frac{n_{\text{ion}}}{Q_{\text{ion}}} \frac{\Lambda^3}{2} \quad (5)$$

with the electron density  $n_e$ , the total ion density  $n_{\text{ion}}$ , the ion partition function  $Q_{\text{ion}}$ , and the thermal electron wavelength

$$\Lambda = \sqrt{\frac{h^2}{2\pi m_e k T_e}} \quad (6)$$

with Planck's constant  $h$ , Boltzmann's constant  $k$ , the electron mass  $m_e$ , and the electron temperature  $T_e$ . The latter temperature is assumed to be in equilibrium with the atomic electronic excitation temperature  $T_{\text{exc}}$  [22]. Equilibrium analysis has shown that, at the enthalpy level at hand, the ions only consist of  $N^+$  and  $O^+$ . Furthermore, when quasineutrality is assumed, the electron density can be calculated by

$$n_e = n_{N^+} + n_{O^+} \quad (7)$$

with the ion number densities  $n_{N^+}$  and  $n_{O^+}$ . Combining Eqs. (5)-(7) yields

$$n_e = \sqrt{\eta_{\infty,O} \cdot Q_{O^+} \cdot \frac{2}{\Lambda^3} \cdot \left(1 + \frac{\eta_{\infty,N} \cdot Q_{N^+}}{\eta_{\infty,O} \cdot Q_{O^+}}\right)} \quad (8)$$

which is used to calculate the electron number density based on the extrapolated virtual states  $\eta_{\infty,N}$  and  $\eta_{\infty,O}$ . As this method is based on an extrapolation, the inclusion of low energy states greatly reduces the sensitivity to uncertainties in the population density measurement for the same reason discussed on the Boltzmann plot in section IIIB 2. The uncertainty of the extrapolation is again the difference between the maximum and minimum possible Boltzmann distributions at the ionization energy (dotted lines in Figs. 11 and 12). Furthermore, the uncertainty in electron temperature is considered which acts on the thermal electron wavelength and the partition functions [45]. One drawback is the restricted applicability in regimes of strong nonequilibrium since the method implies a Saha equilibrium between ions and the energy states of the respective atoms. To quantify the applicability of the method, the ionization relaxation times of atomic nitrogen  $\tau_N$  and atomic oxygen  $\tau_O$  in high temperature plasmas are considered using the works of Kunc and Soon ( $\tau_N < 6 \times 10^{-8}$  s) and Bourdon et al. ( $\tau_O < 7 \times 10^{-8}$  s) [49, 50]. Here, the measured electron temperature and electron density are used to interpolate the tabulated values in the named references. The corresponding distances traveled by particles in the relaxation time within the post-shock region are calculated by multiplying those times with the post-shock gas velocity, which is obtained by normal shock relations [51]. Both atomic species equilibrate with their ions very quickly (within distances  $< 0.1$  mm), mainly due to the very high electron density. However, this value does not include coupling to the chemical relaxation process. Therefore, it is assumed that the Saha equilibrium is only strictly applicable from 0.1 mm behind the start of the equilibrium region.

The NIR spectra feature the strong Balmer- $\alpha$  line of the contaminant species of hydrogen at 656.28 nm. The Stark broadening of this line is very large compared to other atomic lines in the spectrum. Therefore, it is a standard diagnostic method to obtain the electron number density by analyzing the line profile of the Balmer- $\alpha$  line [52]. However, it is assumed that the line is strongly self-absorbing as it is close to the black body limit of the other atoms. Therefore, an electron number density measurement using Stark broadening failed.

As the applicability of some of the methods is restricted to certain regions of the flow, a numerical

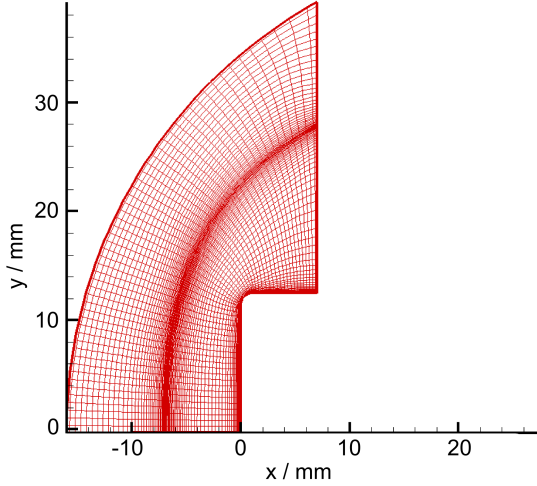


Fig. 13 Numerical grid of the flowfield ( $53 \times 94$  cells).

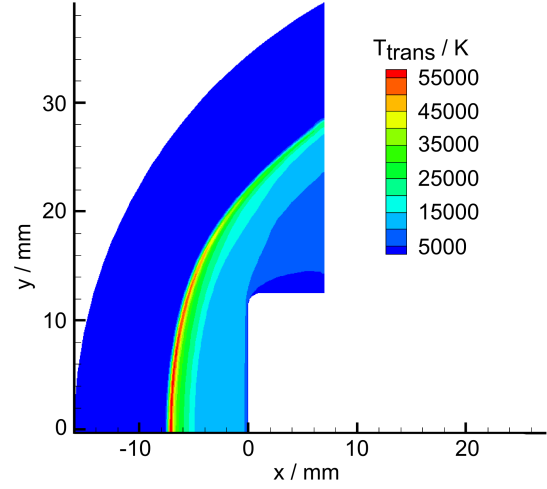


Fig. 14 Numerical solution of the radiation coupled flowfield (translational temperature).

analysis is conducted to provide further insight into the structure of the flowfield and to allow a comparison to the measurement results.

#### D. Numerical rebuilding

This section presents an overview of the detailed numerical analysis conducted using the fully coupled code URANUS which solves the two-dimensional Navier-Stokes equations for Park's 11 species air composition with 47 reactions ( $\text{N}_2$ ,  $\text{O}_2$ ,  $\text{NO}$ ,  $\text{N}$ ,  $\text{O}$ ,  $\text{N}_2^+$ ,  $\text{O}_2^+$ ,  $\text{NO}^+$ ,  $\text{N}^+$ ,  $\text{O}^+$ ,  $\text{e}^-$ ) and a 6 temperature model ( $T_{\text{trans}}$ ,  $T_{\text{rot}}$ ,  $T_{\text{e}}$ ,  $T_{\text{vib},\text{N}_2}$ ,  $T_{\text{vib},\text{O}_2}$ ,  $T_{\text{vib},\text{NO}}$ ) [32, 53]. The temperature of the ionized molecules  $T_{\text{vib},\text{ions}}$  is determined as the weighted average of the vibrational temperatures of the neutral molecules. The thermochemical relaxation is calculated with a CVCV model, the transport coefficients for the viscous fluxes are calculated according to the method of Chapman and Cowling as it is described by Fertig et al. with the collision integrals of Capitelli et al., and a fully catalytic cold wall (300 K) boundary condition is set at the model surface [54, 55]. Optional source terms enable the simulation of rotational symmetric flows. The solver is fully coupled, fully implicit and local timestepping accelerates the convergence to the steady state solution. Inflow conditions are taken from the work of Sheikh (see Table 1) [19]. Emission and absorption coefficients within the flowfield are simulated with the line by line code PARADE and are used to conduct a

loose flowfield-radiation coupling using the Monte-Carlo radiation transport code HERTA [56–58]. In this procedure, the radiative energy source terms are calculated from a converged flowfield. Subsequently, these source terms are applied to URANUS and a new flowfield solution is calculated. The whole procedure is repeated iteratively until convergence is obtained. The electronic excitation temperature, i. e. the parameter controlling the population distribution within electronically excited particles, is not considered in the energy equation of URANUS. However, it is assumed that the modeled electron temperature, i. e. the kinetic energy of the free electrons, corresponds to the electronic excitation temperature which is needed for radiation modeling using PARADE. The calculation is performed on a structured grid with  $53 \times 94$  cells which is shown in Fig. 13. The translational temperature distribution of the radiation coupled flowfield solution is presented in Fig. 14.

A two-dimensional calculation is used due to the large aspect ratio of the model and the grid has been refined at the shock and the boundary layer in order to resolve the steep gradients in the flowfield. As can be seen in Fig. 14, the shock distance is approximately 7.5 mm in front of the model surface which is also observed in the experimental measurements (see Fig. 6). In the following, the radiation coupled numerical results obtained on the stagnation streamline (denoted as 'URANUS') are compared to the respective measurement results.

#### IV. Results

This section presents the thermodynamic properties deduced from the measured spectra as depicted in section III.

##### A. Number densities along the stagnation streamline

Figure 15 presents the measured number densities of atomic nitrogen and oxygen along the stagnation streamline obtained by the summation of the measured ground and low energy states of the respective atoms (see Figs. 11 and 12). Furthermore, the results of the chemical equilibrium code PITOT and the numerical calculation using URANUS are plotted. The measured values are determined using the VUV spectra through the analysis of the radiative transport along the stagnation streamline, i. e. the line of sight of the VUV spectroscopic system. As the radiation

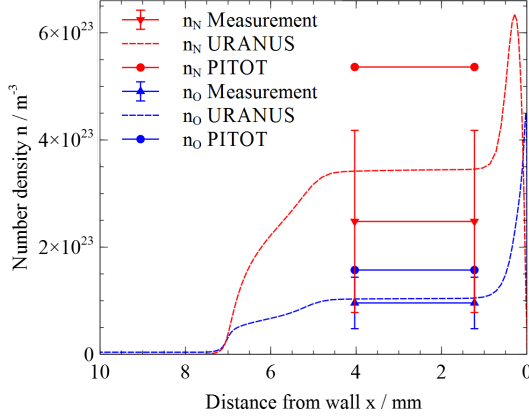


**Fig. 15 Atom number densities along the stagnation streamline.**

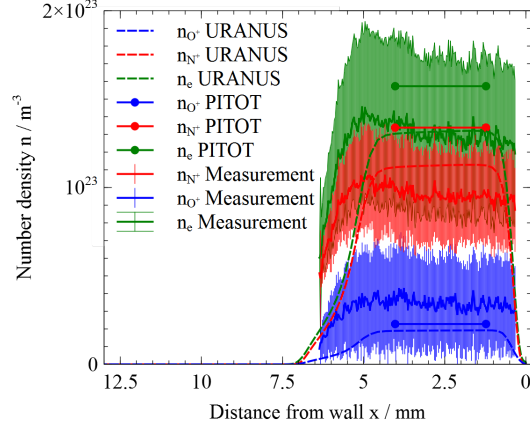


**Fig. 16 Electron and ion number densities along the stagnation streamline.**

reaching the stagnation point is affected mostly by absorption and emission in the equilibrium region behind the shock (refer to Fig. 5), the measured atom density corresponds to this region of the flow. Therefore, the measurement results are plotted as constant values in the equilibrium part of the shock layer. Since the code PITOT applies chemical equilibrium in the calculation of flowfield variables, the respective values are also plotted in the same manner. Significant discrepancies result for atomic nitrogen. The measurement data is over a factor of two smaller than the PITOT result and approximately 30 % smaller than the URANUS result. As discussed in section III A, the uncertainty in the measurement of the nitrogen number density is large since the extrapolation to the ground state is strongly affected by the large uncertainty in the line width. Thus, a reasonably accurate determination of the atomic nitrogen number density failed which is demonstrated by the large error margins (70 %) shown in Fig. 15. In the case of oxygen, the ground state number density is directly accessible through the branching ratio method leading to a smaller uncertainty than the respective nitrogen measurement. The match between URANUS and measurement data is excellent while the PITOT value is approximately 60 % larger than the measurement result and thus just outside the error margins of the method. However, the match between measurement and URANUS data may be a coincidence as the branching ratio of the multiplet responsible for the determination of the atomic oxygen ground state (130.35 nm) is highly sensitive to changes in the instrument function

which is reflected in the uncertainty margins of the measurement result. In conclusion, measurement accuracy of the atomic number density could be improved by a higher spectral resolution and a more accurate database of Stark broadening parameters, this is however beyond the scope of the present study.

Similar measurements in the plasma wind tunnel PWK1 of a condition with comparable enthalpy, but significantly lower pressure (24.4 hPa), were conducted with a higher spectral resolution (0.01 nm) in the VUV regime [26]. The spectral lines measured in the plasma wind tunnel tests are significantly thinner. This is due to the lower electron number density which results in significantly lower Stark broadening. Additionally, the lower atom density results in lower total absorption of the radiation. Therefore, the black body limited component of the self-absorbed line is very small. These mechanisms result in narrow lines which can be easily separated from one another, also due to the higher spectral resolution. This allows the measurement of additional energy states by considering more multiplets in the branching ratio evaluation. Furthermore, the clear separation of single lines within a multiplet is possible, which, as discussed in section III A, improves the measurement accuracy greatly. In the present case of the X2 measurements, the spectral resolution is insufficient to obtain reliable results.

Figure 16 presents the distribution of electron and ion densities along the stagnation streamline obtained by measurement, URANUS simulation, and PITOT simulation. Results obtained with PITOT are larger for all three species compared to the URANUS results, while the ratio between the species is very similar for both numerical results. The measurement results are presented in regions where a sufficient signal to noise ratio of the NIR data exists. The measurement results in the nonequilibrium region (4-7.5 mm) are questionable since the analysis implies a Saha equilibrium which probably does not exist in this flow regime. In the equilibrium region (1-4 mm) the electron density measurement and the respective URANUS calculation result in nearly identical values ( $\pm 6\%$ ). The only difference is a slight decrease of the measured electron density towards the wall, which is primarily due to the same trend in nitrogen ions. One significant difference between measurement and both numerical simulations is the ratio of ions. The measured nitrogen ions are fewer while the oxygen ions are significantly more numerous. However, the numerical solution is

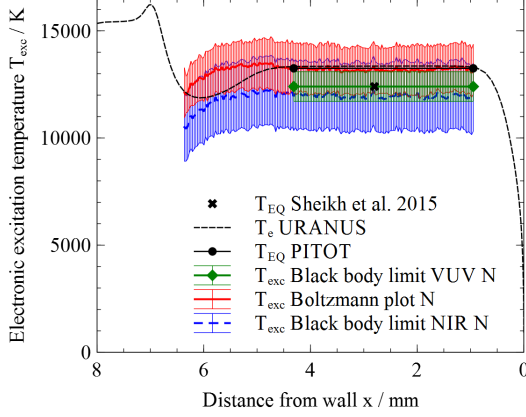


**Fig. 17 Atomic nitrogen electronic excitation temperature along the stagnation streamline.**

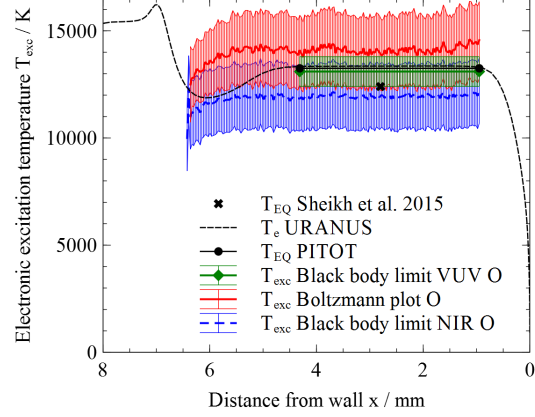


**Fig. 18 Atomic oxygen electronic excitation temperature along the stagnation streamline.**

within the error margins of the measurements. Therefore, a more accurate method is required to investigate the discrepancy between measurement and simulation.

#### B. Electronic excitation temperature along the stagnation streamline

Figures 17 and 18 present the results for the electronic excitation temperature determined by measurement, the electron temperature obtained from the URANUS simulation, and the equilibrium temperature obtained from the PITOT simulation. The different temperature measurement results are labeled according to the analysis method employed. As in the case of the atomic number densities obtained primarily using VUV data, the VUV black body limit temperature is mostly dominated by the equilibrium region of the flow and is therefore plotted as constant in this region. Results are presented in regions where the signal to noise ratio is sufficiently large. Additionally, the temperature measured by Sheikh et al. is presented which was determined by assuming a chemical and thermal equilibrium in the shock layer [59]. Sheikh et al. obtained a temperature by computing the VUV radiation along a constant property flowfield. In the present study the analysis of the measured VUV spectra also considers the spatial distribution of radiation along the line of sight.

The two numerical simulations, URANUS and PITOT, are virtually identical in the equilibrium flow region while all measurement results are within approximately  $\pm 1000\text{ K}$  ( $\pm 8\%$ ) of this value. All spatially resolved measurements exhibit a distinct flat equilibrium region. The NIR black body

limit temperatures are lower than the VUV black body limit temperatures. As the respective measurement method relies on absolute radiance, systematic errors in the calibration and uncertainties in line width can cause this relatively small discrepancy. The Boltzmann plot temperatures are quite high and the oxygen temperature is the highest of all the evaluated temperatures. Since the nitrogen Boltzmann plot features more energy states it is less susceptible to uncertainties in the population densities and therefore regarded as more accurate in comparison to oxygen. This is also clearly visible by comparing the bordering Boltzmann lines in Figs. 11 and 12 respectively, which are directly related to the error margins of the method. The value determined by Sheikh et al. matches the results obtained in this study very well. Considering the spatially resolved temperature measurements, it is evident that the assumption of a constant property flowfield is valid due to the large equilibrium region. Interestingly, a small corridor (12400–13100 K) exists just below the equilibrium temperature 13250 K, where the uncertainty margins of all methods overlap.

A significant difference between the URANUS calculation result and the measurement is the temperature rise in the shock. The measurements show a steady rise of the electronic temperature as it has been observed in previous experimental investigations [21]. In contrast, the numerical simulation predicts a higher than equilibrium electron temperature ahead of the shock which relaxes towards equilibrium at approximately 4.5 mm. The measurement results show that equilibrium is already reached by 5.5 mm. The different sizes of the equilibrium region indicate that the thermal relaxation is faster than modeled in the numerical simulation. The higher than equilibrium temperature in front of the shock predicted by the URANUS simulation has small impact on the post shock flowfield since it describes the properties of only very few free electrons (refer to Fig. 16). For the measurement, free electron temperature and electronic excitation temperature are assumed to be the same [22]. However, in regions of small electron density, e. g.  $x > 7.5$  mm in Fig. 6, the excitation of electronic states is very ineffective and therefore emission spectroscopic measurements do not detect emission.

This study revealed that, as expected, the driving source of the radiative heat flux from the VUV spectral region are the atomic lines of N and O. Furthermore, the measured population densities of the different atomic states proved that the flowfield is highly self-absorbing. As the radiative

transport is highly dependent on the lineshape, the spatial distribution of the physical parameters relevant for the respective broadening mechanisms within the flowfield is essential. For superorbital re-entry flowfields, as in the present case, Stark broadening is the most important factor. Stark broadening depends on electron density and electron temperature, therefore, these two parameters are of high importance for the correct prediction of the radiative heating to a re-entry vehicle. The study showed that both parameters exhibit a rather flat distribution in the equilibrium region which is the primary source of the radiative heat flux. The measurements provide an opportunity to improve the modeling of spectral lines and thus mitigate uncertainties in radiative heating to re-entry vehicles.

## V. Conclusion

Experiments of a superorbital flow with a flight equivalent velocity of 12.2 km/s and a free stream density of  $1 \times 10^{-3} \text{ kg/m}^3$  have been conducted in the X2 expansion tube at the Centre for Hypersonics of the University of Queensland. Optical emission spectroscopic measurements in the vacuum ultraviolet spectral region have been carried out by viewing the flow through the stagnation point of a flat model. Optical emission spectroscopic measurements of the stagnation streamline in the near infrared spectral region have been accomplished by viewing the flow from the side. Particle densities of atomic nitrogen and oxygen are obtained by analyzing the branching ratio of self-absorbed atomic multiplets and using an extrapolation to the ground state. The electronic excitation temperature is deduced utilizing the Boltzmann plot method and the black body limit in both measured spectral regions. Electron and ion densities are calculated by applying the Saha equation and adding to the measured Boltzmann plot. The flowfield is numerically rebuilt using the nonequilibrium code URANUS, with radiation-flowfield coupling using the radiation database PARADE and the radiative transfer code HERTA.

Discrepancies in atomic nitrogen number density in the equilibrium region exist between nonequilibrium numerical simulation, equilibrium calculation and the measurements. The measurement uncertainty could be reduced by using a higher spectral resolution, however, this is beyond the scope of this study. Atomic oxygen number density and electron density measurements in the equilibrium region match numerical results closely. Electronic excitation temperature measurements

exhibit a large equilibrium region close to the temperature deduced from equilibrium calculations and numerical results. However, measurements indicate that the relaxation process is faster than modeled in the numerical simulation.

### Acknowledgments

The authors gratefully acknowledge the funding by the DAAD through the grant 81027188. The authors would like to thank the colleagues from the Centre for Hypersonics and the High Enthalpy Flow Diagnostics Group for the dedicated help and the welcoming atmosphere. **Additionally, the authors would like to acknowledge the input of the reviewers whose comments and suggestions increased the quality of the paper significantly.**

### References

- [1] Gnoffo, P. A., “Planetary-Entry Gas Dynamics,” *Annual Review of Fluid Mechanics*, Vol. 31, 1999, pp. 459–494.
- [2] Johnston, C. O., Mazaheri, A., Gnoffo, P. A., Kleb, B., Sutton, K., Prabhu, D., Brandis, A. M., and Bose, D., “Assessment of Radiative Heating Uncertainty for Hyperbolic Earth Entry,” *42nd AIAA Thermophysics Conference*, June 2011.
- [3] Gupta, R. N., “Aerothermodynamic Analysis of Stardust Sample Return Capsule with Coupled Radiation and Ablation,” *Journal of Spacecraft and Rockets*, Vol. 37, No. 4, July 2000, pp. 507–514.
- [4] Ried, R. C., Rochelle, W. C., and Milhoan, J. D., “Radiative Heating to the Apollo Command Module: Engineering Prediction and Flight Measurement,” Tech. Rep. NASA-TM-X-58091, Johnson Space Center, April 1972.
- [5] Hoshizaki, H. and Lasher, L. E., “Convective and Radiative Heat Transfer to an Ablating Body,” *Thermophysics Conference*, No. AIAA-67-327, AIAA, 1967.
- [6] Johnston, C. O., Gnoffo, P. A., and Mazaheri, A., “Influence of Coupled Radiation and Ablation on the Aerothermodynamic Environment of Planetary Entry Vehicles,” *Radiation and Gas-Surface Interaction Phenomena*, Vol. 218 of *RTO Lecture Series*, 2013.
- [7] Brandis, A. M. and Johnston, C. O., “Characterization of Stagnation-Point Heat Flux for Earth Entry,” *45th AIAA Plasmadynamics and Lasers Conference*, Atlanta, GA, June 2014.
- [8] Zander, F., Marynowski, T., and Löhle, S., “High-Speed Imaging of a Steady State CO<sub>2</sub> Plasma Flow,” *Journal of Thermophysics and Heat Transfer*, 2015, submitted.

- [9] Löhle, S., Staebler, T., Reimer, T., and Cefalu, A., “Photogrammetric Surface Analysis of Ablation Processes in High Enthalpy Air Plasma Flow,” *30th Aerodynamic Measurement Technology and Ground Testing Conference*, AIAA, 2014, accepted for publication.
- [10] Marynowski, T., Löhle, S., and Fasoulas, S., “Two-Photon Absorption Laser-Induced Fluorescence Investigation of CO<sub>2</sub> Plasmas for Mars Entry,” *AIAA Journal of Thermophysics and Heat Transfer*, Vol. 28, No. 3, 2014.
- [11] Löhle, S., Hermann, T., Zander, F., Fulge, H., and Marynowski, T., “Ablation Radiation Coupling Investigation in Earth Re-entry Using Plasma Wind Tunnel Experiments,” *30th Aerodynamic Measurement Technology and Ground Testing Conference*, AIAA, 2014.
- [12] Lu, F. K. and Marren, D. E., editors, *Advanced Hypersonic Test Facilities*, Vol. 198 of *Progress in Astronautics and Aeronautics*, AIAA, 2002, ISBN 1-56347-541-3.
- [13] Grinstead, J. H., Driver, D. M., and Raiche, G. A., “Optical Diagnostics Development for the Ames Arcjet Facilities,” *40th Aerospace Sciences Meeting and Exhibit*, Reno, Nevada, January 2002.
- [14] Kolesnikov, A. F., “Extrapolation from High Enthalpy Tests to Flight Based on the Concept of Local Heat Transfer Simulation,” *Measurement Techniques for High Enthalpy and Plasma Flows*, No. 8B, VKI, RTO — Research and Technology Organization, Rhode-Saint-Genese, Belgium, 1999.
- [15] Sakraker, I., Turchi, A., and Chazot, O., “Hypersonic Aerothermochemistry Duplication in Ground Plasma Facilities: A Flight-to-Ground Approach,” *Journal of Spacecraft and Rockets*, 2015.
- [16] Turchi, A., Matesanz Saiz, J. J., Magin, T. E., and Chazot, O., “On the Flight Extrapolation of Stagnation-Point Ablative Material Plasma Wind Tunnel Tests,” *8th European Symposium on Aerothermodynamics for Space Vehicles*, 2015.
- [17] Morgan, R., “Superorbital expansion tubes,” *21st International Symposium on Shock Waves*, July 1997.
- [18] Potter, D., *Modelling of radiating shock layers for atmospheric entry at Earth and Mars*, Ph.D. thesis, The University of Queensland, St. Lucia, Australia, May 2011.
- [19] Sheikh, U., *Re-Entry Radiation Aerothermodynamics in the Vacuum Ultraviolet*, Ph.D. thesis, University of Queensland, 2014.
- [20] Johnston, C. O., Samareh, J., and Brandis, A. M., “Aerothermodynamic Characteristics of 16-22 km/s Earth Entry,” *45th AIAA Thermophysics Conference*, Dallas, TX, June 2015.
- [21] Eichmann, T., *Radiation Measurements in a Simulated Mars Atmosphere*, Ph.D. thesis, University of Queensland, 2012.
- [22] Park, C., *Nonequilibrium Hypersonic Aerothermodynamics*, John Wiley & Sons, 1990.

- [23] McIntyre, T., Khan, R., Eichman, T., Upcroft, B., and Buttsworth, D., “Visible and Near Infrared Spectroscopy of Hayabusa Reentry Using Semi-Autonomous Tracking,” *Journal of Spacecraft and Rockets*, Vol. 51, No. 1, Jan. 2014, pp. 31–38.
- [24] McIntyre, T., Eichman, T., Jacobs, C., Potter, D., McGilvray, M., Jacobs, P., and Morgan, R., “Shock Tube and Expansion Tunnel Measurements of High Temperature Radiating Flows,” *4th International Workshop on Radiation of High Temperature Gases in Atmospheric Entry*, ESA, 2010.
- [25] Sheikh, U., Morgan, R., Zander, F., Eichman, T., and McIntyre, T., “Vacuum Ultraviolet Emission Spectroscopy System for Superorbital Reentries,” *18th AIAA/3AF International Space Planes and Hypersonic Systems and Technologies Conference*, AIAA, 2012.
- [26] Hermann, T., Zander, F., Fulge, H., Löhle, S., and Fasoulas, S., “Characterization of a Re-entry Plasma Wind Tunnel Flow with Vacuum Ultraviolet to Near Infrared Spectroscopy,” *Journal of Thermophysics and Heat Transfer*, 2015, submitted.
- [27] Fletcher, D. G., “Nonintrusive Diagnostic Strategies for Arcjet Stream Characterization,” Vol. Measurement Techniques for High Enthalpy and Plasma Flows, Oct. 1999.
- [28] Laity, G., *A Radiative Model for Determining Plasma Dissociation Using Vacuum Ultraviolet Self-Absorption Spectroscopy*, Ph.D. thesis, Texas Tech University, May 2013.
- [29] Brandis, A. M., Johnston, C. O., Cruden, B., Prabhu, D., Wray, A. A., Liu, Y., Schwenke, D. W., and Bose, D., “Validation of CO<sub>4</sub>th positive radiation for Mars entry,” *Journal of Quantitative Spectroscopy Radiative Transfer*, Vol. 121, 2013, pp. 91–104.
- [30] van der Sijde, B. and van der Mullen, J. A. M., “Temperature Determination in non-LTE Plasmas,” *Journal of Quantitative Spectroscopy and Radiative Transfer*, Vol. 44, No. 1, 1990, pp. 39–46.
- [31] James, C., Gilfind, D. E., Morgan, R., Jacobs, P., and Zander, F., “Designing and simulating high enthalpy expansion tube conditions,” *Pacific International Symposium on Aerospace Technology*, 2013.
- [32] Fertig, M. and Herdrich, G., “The Advanced URANUS Navier-Stokes Code for the Simulation of Nonequilibrium Re-entry Flows,” ISTS-Paper 2008-e-20, 26th International Symposium on Space Technology and Science, Hamamatsu, Japan, 2008.
- [33] Gordon, S. and McBride, B. J., “Computer Program for Calculation of Complex Chemical Equilibrium Compositions and Applications,” Reference Publication 1311, NASA, 1996.
- [34] Sheikh, U., Ibrahim, M., Lewis, S., Wei, H., Morgan, R., and McIntyre, T., “Filtered Two-Dimensional Imaging in the X2 Expansion Tube,” *6th International Workshop on Radiation of High Temperature Gases in Atmospheric Entry*, St Andrews, UK, Nov. 2014.

- [35] Jacobs, C., *Radiation in low density hypervelocity flows*, Ph.D. thesis, The University of Queensland, 2011.
- [36] Brandis, A. M., Johnston, C. O., Cruden, B., Prabhu, D., and Bose, D., "Uncertainty Analysis and Validation of Radiation Measurements for Earth Reentry," *Journal of Thermophysics and Heat Transfer*, Vol. 29, No. 2, 2015, pp. 209–221.
- [37] Sheikh, U., Morgan, R., and McIntyre, T., "Self-absorption of vacuum ultraviolet radiation in super-orbital flows." *5th International Workshop on Radiation of High Temperature Gases in Atmospheric Entry*, 2012.
- [38] Stirn, R., *Emissionsspektroskopische Untersuchungen der Wechselwirkung eines Freistrahls mit Hitzeschutzmaterialien*, Ph.D. thesis, Institut für Plasmaforschung der Universität Stuttgart, Dec. 2005.
- [39] Laity, G., Fierro, A., Dickens, J., Neuber, A., and Frank, K., "Simultaneous measurement of nitrogen and hydrogen dissociation from vacuum ultraviolet self-absorption spectroscopy in a developing low temperature plasma at atmospheric pressure," *Applied Physics Letters*, Vol. 102, No. 184104, May 2013.
- [40] Boffard, J. B., Jung, R. O., Lin, C. C., and Wendt, A. E., "Measurement of metastable and resonance level densities in rare-gas plasmas by optical emission spectroscopy," *Plasma Sources Science and Technology*, Vol. 18, June 2009, pp. 1–11.
- [41] Laux, C. O., *Optical Diagnostics and Radiative Emission of Air Plasmas*, Ph.D. thesis, Stanford University, 1993.
- [42] Johnston, C. O., Hollis, B. R., and Sutton, K., "Spectrum Modeling for Air Shock-Layer Radiation at Lunar-Return Conditions," *Journal of Spacecraft and Rockets*, Vol. 45, No. 5, 2008, pp. 865–878.
- [43] National Institute of Standards and Technology, <http://physics.nist.gov/PhysRefData/ASD>, 2014.
- [44] Laity, G., Fierro, A., Dickens, J., Frank, K., and Neuber, A., "A passive measurement of dissociated atom densities in atmospheric pressure air discharge plasmas using vacuum ultraviolet self-absorption spectroscopy," *Journal of Applied Physics*, Vol. 115, No. 123302, March 2014.
- [45] Taylor, J. R., *An Introduction to Error Analysis*, University Science Books, Sausalito, California, second edition ed., 1982.
- [46] Johnston, C. O. and Brandis, A. M., "Features of Afterbody Radiative Heating for Earth Entry," *11th AIAA/ASME Joint Thermophysics and Heat Transfer Conference*, Atlanta, GA, 2014.
- [47] Park, C., "Calculation of Nonequilibrium Radiation in AOTV Flight Regimes," *AIAA 22nd Aerospace Sciences Meeting*, Jan. 1984.

- [48] The only exception is the resonance multiplet at 120.00 nm which is overlapped by neighboring lines. However, the black body limited part of the line is significantly broader than the spectral resolution. Therefore, the measured peak value of the line is directly applied as the black body limit.
- [49] Kunc, J. A. and Soon, W. H., "Collisional-Radiative Nonequilibrium in Partially Ionized Atomic Nitrogen," *Physical Review A*, Vol. 44, 1989, pp. 5822–5843.
- [50] Bourdon, A., Téréziak, Y., and Vervisch, P., "Ionization and Recombination Rates of Atomic Oxygen in High-Temperature Air Plasma Flows," *Phys. Rev. E*, Vol. 57, Apr 1998, pp. 4684–4692.
- [51] Anderson, J. D., *Hypersonic and High-Temperature Gas Dynamics, 2nd Edition*, AIAA Education Series, 2nd ed., 2006.
- [52] Ivkovic, M., Jovicevic, S., and Konjevic, N., "Low electron density diagnostics: development of optical emission spectroscopic techniques and some applications to microwave induced plasmas," *Spectrochimica Acta Part B*, Vol. 59, No. 5, May 2004, pp. 591–605.
- [53] Park, C., "Convergence of Computation of Chemical Reacting Flows," *Progress in Astronautics and Aeronautics*, Vol. 103, 1986, pp. 478–513.
- [54] Fertig, M., Dohr, A., and Frühauf, H.-H., "Transport Coefficients for High Temperature Nonequilibrium Air Flows," *AIAA Journal of Thermophysics and Heat Transfer*, Vol. 15, No. 2, April 2001, pp. 148–156.
- [55] Capitelli, M., Gorse, C., Longo, S., and Giordano, D., "Transport Coefficients of High-Temperature Air Species," AIAA-Paper 98-2936, 7th Joint Thermophysics and Heat Transfer Conference, Albuquerque, New Mexico, USA, June 1998.
- [56] Gogel, T. H., Dupuis, M., and Messerschmid, E. W., "Radiation Transport Calculation in High Enthalpie Environments for Two-Dimensional Axisymmetric Geometries," *Journal of Thermophysics and Heat Transfer*, Vol. 8, No. 4, 1994, pp. 744–750.
- [57] Liebhart, H., Herdrich, G., and Merrifield, J. A., "Advances for Radiation Modeling for Earth Re-entry in PARADE: Application to the STARDUST Atmospheric Entry," *43rd AIAA Thermophysics Conference*, AIAA, 2012.
- [58] Löhle, S., Brandis, A., Hermann, T., and Peter, J., "Numerical Investigation of the Re-entry Flight of Hayabusa and Comparison to Flight and Ground Testing Data," *43rd AIAA Thermophysics Conference*, AIAA, New Orleans, LA, 2012.
- [59] Sheikh, U., Morgan, R., and McIntyre, T., "Vacuum Ultraviolet Spectral Measurements for Superorbital Earth Entry in X2 Expansion Tube," *AIAA Journal*, 2015.